Rolling-Joint Design Optimization for Tendon Driven Snake-like Surgical Robots

Pierre Berthet-Rayne[1], Konrad Leibrandt[1], Kiyoung Kim[1],
Carlo A. Seneci[1], Jianzhong Shang[1] and Guang-Zhong Yang[1] *Fellow IEEE*

***Abstract*— The use of snake-like robots for surgery is a popular choice for intra-luminal procedures. In practice, the requirements for strength, flexibility and accuracy are difficult to be satisfied simultaneously. This paper presents a computational approach for optimizing the design of a snake-like robot using serial rolling-joints and tendons as the base architecture. The method optimizes the design in terms of joint angle range and tendon placement to prevent the tendons and joints from colliding during bending motion. The resulting optimized joints were manufactured using 3D printing. The robot was characterized in terms of workspace, dexterity, precision and manipulation forces. The results show a repeatability as low as 0.9 mm and manipulation forces of up to 5.6 N.**

I. Introduction

Snake-like robots have the potential to improve navigation and minimize access trauma for intra-luminal surgical procedures. These robots often use bio-inspired locomotion with a flexible actuated body, allowing the entire system to navigate inside a human anatomy and perform surgical tasks. They present many advantages compared to conventional surgical robots. First, their long and narrow shape allows them to reach confined regions and deep-seated lesions. Second, their body is flexible and can follow natural pathways, offering a broad range of potential surgical procedures through natural orifices. Finally, they require fewer incisions or even no incision leading to less patient trauma. It is anticipated that the evolution of snake-like robots will have a positive impact on minimally invasive surgery [1], [2], [3].

In general, surgical snake robots should have the following features: a narrow body to navigate through small incisions or natural orifices. It also needs to have locomotion that is amenable to local anatomical constraints, *e.g.*, path following and navigate within a prescribed working volume. These require redundant degrees of freedom (DOF) to allow for full retroflexion and navigation through natural human pathways. They should be equipped with high fidelity vision or stereovision and adequate lighting. As the objective is to perform surgical tasks, the system should have multiple internal channels and have a complete range of tools such as graspers, cauterization *etc.* which can be easily exchanged during surgical procedures. The manipulation forces should be sufficient for tissue manipulation. Other features include the incorporation of a suction irrigation channel and integrated sensing and imaging, allowing tissue palpation and multispectral imaging to reveal cancerous or abnormal tissue to the human eye. Ultimately, such devices could also be patient specific to ensure a custom fit to uncommon anatomies. Thus far, there are multiple snake-like devices being developed in the research community and industry. Burgner-Kahrs *et al.* introduced a review on existing continuum robots designed for surgical applications [4]. According to this review, existing robotic devices can be categorized in two groups: systems with internal actuation, and systems with external actuation, where the actuation source is placed outside of the body [4]. Internal actuation methods include micro-motors, pneumatic, and shape memory alloy. External actuation schemes include tendons, backbone and concentric tubes. Designing a new snake-like robotic platform requires an exhaustive study of existing actuation methods to evaluate their strengths and limitations. Internal actuation such as micro-motors [5], [6], [7], [8] for instance offer modularity and fine precision, however, the available forces are limited by the size of the embedded micro-motors thus reducing the space for tools. Pneumatic actuation of flexible structures has advantages such as compliance, elongation and large forces [9], but they provide a limited space for tool channels and often have a large outer diameter. Shape memory alloy actuated systems can have a small diameter, as less mechanical moving parts are required, but their actuation is often slow and limited in range and forces [10]. Concentric

Fig. 1: Picture of the *i²Snake* (Intuitive Imaging Sensing Navigated and Kinematically Enhanced robot) prototype. The *i²Snake* is a robotic platform with a flexible body and equipped with vision, lighting and two robotic tools.

[1]The Hamlyn Centre for Robotic Surgery, Imperial College London, London, United Kingdom

Corresponding author: ptb14 at imperial.ac.uk

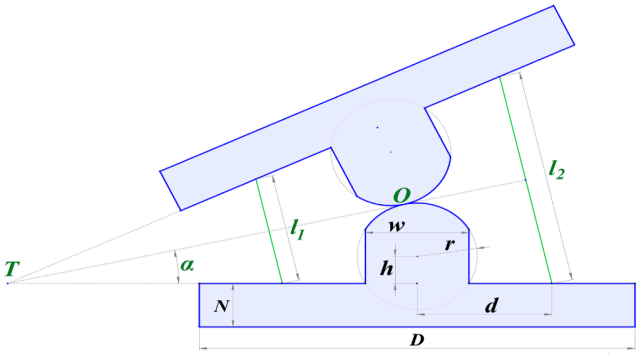

Fig. 2: Cross section of a rolling-joint. As the joint moves, the circular surfaces roll against each other and change the contact point O. This figure depicts the parameters (in black) and state variables (in green).

tube robots have the advantage of miniature size [11], but their application is mainly focused on carrying a single tool at a time, hence they are more suited for specialized single tool applications. Backbone architectures have the advantage of a continuum curvature and a small diameter, which comes at the cost of reduced available space for tool channels and are therefore more suited for robotic tools as well [12], [13]. Finally, tendon-driven robots with serial links can generate large forces while providing room for tool channels [14], however, they tend to have elasticity and stretch over time leading to backlash. However, studies on tendon and backlash modeling [15], [16] and mechanical actuation [17] can compensate for these issues.

The purpose of this paper is to introduce the design of a novel multi-tool snake-like robot for minimally invasive surgery: the *i²Snake* [18], [19] combining a redundant flexible robotic body and flexible robotic instruments. The device requirements include inner space for multiple tools and forces sufficiently high to manipulate bulk tissue. As a result, a tendon-driven architecture with serial links offers the best trade-off for such application. More specifically, the work presented uses an optimized rolling-joint design. The rolling-joint is a bio-inspired mechanism that consists of two circular or ellipsoid surfaces rolling against each other. It can be found in bone joints of many living species including the human knee and phalanges. Some of its advantages include a hollow core and large force transmission. The rolling-joint has been used as snake-like manipulator [14], compliant mechanism [20], robot fingers [21] and surgical graspers [22]. Suh *et al.* presented a thorough study of the rolling-joint characteristics applied to planar and compliant continuum robot design [23]. The focus of this paper is to optimize the design of the rolling-joint for 3D motion, and to build a redundant snake-like robot for minimally invasive surgery as shown in Fig. 1.

II. Robot Modeling

A. Planar Rolling-Joint Model.

This section introduces the relation between the tendon variation and the resulting rolling-joint angle while moving in a single plane. The rolling-joint properties consist of joint parameters and motion variables represented in Fig. 2. The parameters are the rolling-joint radius r and the hinge height h representing the height of the center of the circular shape of the joint. Other parameters include the hinge width w, the tendon distance to the center of the joint d, the joint diameter D and the joint height N. The rolling-joint angle is represented by the state variable α and the virtual intersection between the two sections of the joint is T. The roll intersection O is located at the point of contact between the two rolling surfaces. Finally, the left and right tendons used to actuate the joint are represented by l_1 and l_2. Tuning the parameters will have an impact on the range of motion, the variation of the tendon length, the stability of the joint and the force available. One of the properties of the rolling-joint is that the point of contact O moves as the joint is rolling. This makes the model of the rolling-joint more complex than a standard revolute joint where the center of rotation is constant. Typical approaches for rolling-joint modeling consider the remote intersection point T to calculate the relation between the tendon variation and the resulting joint angle. However, this method introduces a singularity when the two joints are parallel to each other, as this intersection does not exist anymore. Another approach using Thales intercept theorem derived similarly to the model presented in [23] is shown below:

$$l_1 = 2\,r + r\,h\,\cos(\alpha) - 2\,d\,\sin(\alpha) \quad (1)$$

$$l_2 = 2\,r + r\,h\,\cos(\alpha) + 2\,d\,\sin(\alpha) \quad (2)$$

The rolling-joint study presented in [23] showed that the tendon variation could be made symmetric if $h = 0$ resulting in the center of the circle of the rolling-joint being coincident with the center of the base of the joint. However, according to the same study, setting $h = 0$ does not guarantee smooth bending without buckling in the case of multiple planar rolling-joints arranged in series [23]. Nonetheless, the design proposed in this paper introduces a different architecture and rolling-joint arrangement where each joint is actuated by individual tendons, hence avoiding the risk of buckling. Therefore, setting $h = 0$ simplifies the model and presents many advantages in terms of stability of the joint and in the simplicity of the actuation of the tendons. Standard antagonistic tendon-driven revolute joints have an asymmetric tendon pathway, meaning that the tendon variation on one side of the joint is different from the one on the opposite side during planar movement, which will lead to joint instability and slack [2]. This can be partly compensated by using asymmetric actuation units, but this is at the cost of more complex and hence more cumbersome tendon actuation systems. In this context, the optimization approach presented will consider a symmetrically actuated joint with $h = 0$. To model the rolling-joint for planar movement (1), (2) are sufficient. The next section will introduce a model for two consecutive orthogonal joints moving in 3D space.

B. 3D Rolling-Joint Model.

In the case of two consecutive rolling-joints arranged orthogonally, the resulting motion will be in 3D space.

The proposed rolling-joint arrangement uses a 'floating configuration' where the middle link is floating between two rolling-joint arranged orthogonally as shown in Fig. 3. In this configuration, two pairs of antagonistically actuated tendons are running through a first link, then pass through the second link, and finally stop inside the third link. The tendon pairs are arranged in a cross configuration, and the motion of one cable c_1 or c_2 will induce a combined motion of both rolling-joints. The reason for this arrangement is to avoid having tendons going through the rolling part of the joint and increase stability. Using (1), (2), it is possible to derive the equations relating the combined tendon variation of two pair of tendons to the two joints. As mentioned in the previous section, the tendon variation is made symmetric with $h = 0$, meaning capstans are sufficient to symmetrically actuate the joints. The bottom rolling-joint will have an angle α_{bot} and a tendon distance to the center d_{bot}. The top joint will have an angle α_{top} and a tendon distance to the center d_{top}. To ensure independent motion of the joints, the tendons must be actuated in pairs. To calculate the tendon displacement corresponding to a desired joint angle based on the cross-configuration tendons, one must follow the following steps and equations. The first step consists of expressing the desired joint angle θ_i, coming from the Denavit-Hartenberg parameters, into the corresponding rolling-joint angle α with:

$$\theta_1 = 2\,\alpha_{bot} \text{ and } \theta_2 = 2\,\alpha_{top} \tag{3}$$

The tendon length on each side of the rolling-joint presented in the planar model (1), (2) is now expressed for the bottom joint: l_{1bot} and l_{2bot} and the top joint: l_{1top} and l_{2top}, and are depicted in Fig. 3. The following step consist of expressing the cross configuration tendon length on each side of each bottom and top joint: L_{1A} and L_{1B} for the cable c_1 connected to motor 1, and L_{2A} and L_{2B} for the cable c_2 connected to motor 2. Only the relative tendon variation is of interest in the following equations, therefore constant parameters such as N are not represented:

$$L_{1A} = l_{1bot} + l_{1top} \quad \text{and} \quad L_{1B} = l_{2bot} + l_{2top} \tag{4}$$

$$L_{2A} = l_{2bot} + l_{1top} \quad \text{and} \quad L_{2B} = l_{1bot} + l_{2top} \tag{5}$$

The resulting tendon variations for the antagonistic actuation Δ_1 and Δ_2 for tendon 1 and 2 are calculated as follow:

$$\Delta_1 = L_{1A} - L_{1B} \text{ and } \Delta_2 = L_{2A} - L_{2B} \tag{6}$$

The motor angles β_1 and β_2 for each motor 1 and 2 respectively equipped with a capstan of radius R can be calculated as follow:

$$\beta_1 = \frac{\Delta_1}{(2\,R)} \text{ and } \beta_2 = \frac{\Delta_2}{(2\,R)} \tag{7}$$

With (1) - (7) we can express the rolling-joint angles as a function of the motor angle:

$$\alpha_{bot} = \arcsin\left(\frac{R\,(\beta_2 - \beta_1)}{4\,d}\right) \tag{8}$$

$$\alpha_{top} = \arcsin\left(\frac{R\,(-\beta_2 - \beta_1)}{4\,d}\right) \tag{9}$$

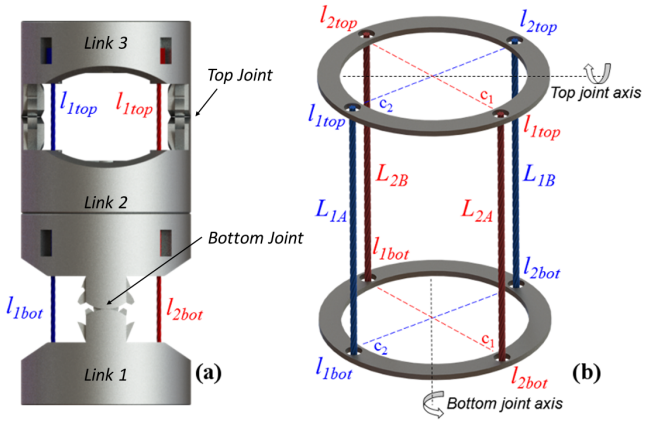

Fig. 3: (a) Proposed 'floating configuration' of rolling-joints arranged orthogonally. (b) Schematic with joint axis. The actuation is made in cross configuration: diametrically opposed cable pairs c_1 and c_2 will control both the top and bottom joints angles.

The proposed equations are sufficient to model the rolling-joint for 3D movement and are used in the next sections to optimize the multiple joint parameters.

III. Rolling-Joint Design Optimization

A. Rolling-Joint Stability

The rolling-joint presents many advantages such as low friction, large force transmission capabilities while having a hollow core for internal channels. However, standard rolling-joints have a significant drawback: the two curved parts can slip, resulting in control inaccuracies or even a dislocated joint. Three different kinds of slipping can occur. Using Fig. 2 as a reference to describe the different types of slipping, the first one is the 'lateral-slip' when the top rolling part rolls too far and falls of the bottom one, resulting in a dislocated joint. The second type of slipping is the 'longitudinal-slip' which could occur if external side forces are exerted on one of the joint, which would result again in a dislocated joint. The final type of slipping is the 'rolling-slip' when the two surfaces skid against each other, resulting in an uncontrolled rolling motion and inaccuracies. To overcome these limitations, a new bi-stable synchronous rolling-joint design is proposed. The solution consists of using a spur gear sandwiched between two rolling surfaces combined with four tendons. The spur gear can overcome both the longitudinal-slip and the rolling-slip while the four tendons, in addition to the gear, can prevent the lateral slip. The design is presented in Fig. 3. The stability is a well known limitation of the rolling-joint and has been previously addressed using a pin or a single tooth [24], but without considering the full range of the joint motion that would result in the tooth or pin being out of range leading to the risk of asynchronous motion or dislocation. Other approaches such as [25], induce a voluntary slippage resulting in a standard pin joint motion and do not qualify as rolling-joint anymore. [23] use a tendon going through the rolling surface, but this approach only reduces large slippage. The use of a spur gear sandwiched between two rolling surfaces ensures that both surfaces roll

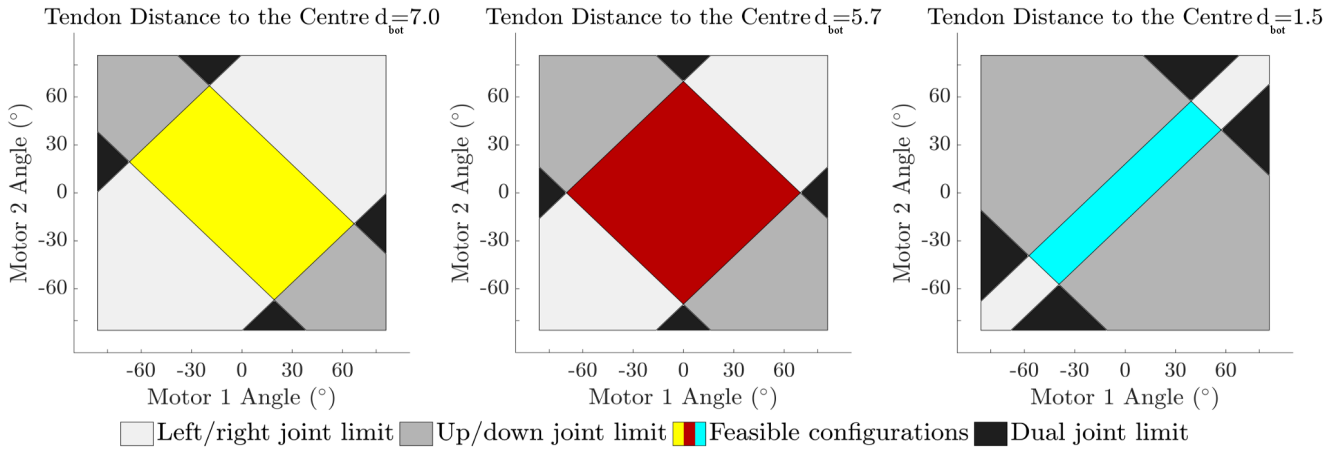

Fig. 4: Joint range results for different tendon pathway locations. The exploration is performed in motor space by varying the motor angle. In the left and right figures, the feasible configurations are significantly reduced and must be avoided during the design of a rolling-joint. The middle figure shows the best tendon pathway location resulting in a larger joint range.

in a controlled motion, and that they do not slip. This result in a smooth controlled motion across the full range of the joint. In the context of this paper, the spur gear pressure angle was set to 20°, the pitch circle is equal to the rolling-joint radius r, and the amount of teeth was set to 12. To optimize the rolling-joint range of motion, an optimization algorithm is used to calculate the various joint parameters. The optimization algorithm considers the tendon placement as well as collisions in the optimization process and is described in the following sections.

B. Tendon Pathway Optimization.

One of the key design parameter in snake-like robots is the tendon placement within the joints. There are multiple parameters combinations of tendon location which will impact the inner channel size, the joint range and the torque delivery. In the case of standard revolute joints, it is common to spread all the tendons in the outer circular area of the joint [24], [26]. However, in the case of the proposed rolling-joint arrangement, such placement can reduce the joint range.
As stated earlier, four tendons are required to control two joints arranged orthogonally. This section presents an exploration algorithm that will simulate different tendon position d and calculate their corresponding joint range $\Delta\alpha$. The joint angle of a specific tendon placement is computed using (8), (9). As shown in Fig. 3, the proposed 'floating' arrangement uses two orthogonally arranged rolling-joints. An iterative process is used to alter the tendon position d within the physical dimension of the joint. For each new tendon position, a secondary explorative sampling of the joint space is performed where for each sampled joint-configuration, the pulling of the tendons is simulated, and with (8), (9) as objective functions, the feasibility of the respective configuration is tested. A valid configuration (within joint and tendon limit) is marked as such, and configurations resulting in joint limit are marked infeasible. A representation of the simulation result is shown in Fig. 4. This figure shows the motor pair displacement angles and the resulting feasible joint configurations for a specific tendon pathway position. To ensure feasible inputs for the actuators, the input parameters of the optimization were chosen to be in motor angle space rather than tendon length space. The motor angles β_1 and β_2 are dependent on the capstan radius R used for actuation. Different tendon pathway locations will result in different areas of feasible configurations where a large area is desired since it represents a large joint range. Fig. 4 shows three sampled tendon pathway locations; on the left, a slice with limited range for the left/right motion is shown while on the right, a slice with up/down limitation is depicted. The center shows the maximum joint range achievable. To visualize the optimization problem, all the computed slices were stacked and visualized as a heat map in Fig. 5. Each slice was given a score based on the area of the feasible space. The color represents the optimization objective criteria of maximizing the feasible area (discretization step size of 0.015 rad for the motor angle, and 0.035 mm for the tendon distance to the center). For a joint diameter of 16 mm the tendon position reaches a maximum when the tendon distance to the center is chosen as d=5.66 mm, corresponding to the tendons being equidistant to the hinges for the left/right and up/down motion. Although this result seems straightforward, this sim-

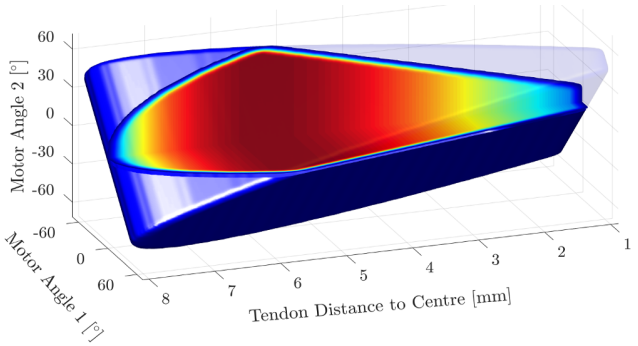

Fig. 5: 3D heat map of the exploration of the tendon position. The exploration is performed in motor space by varying the motor angle and checking for collisions. Areas in dark red show an increased joint range.

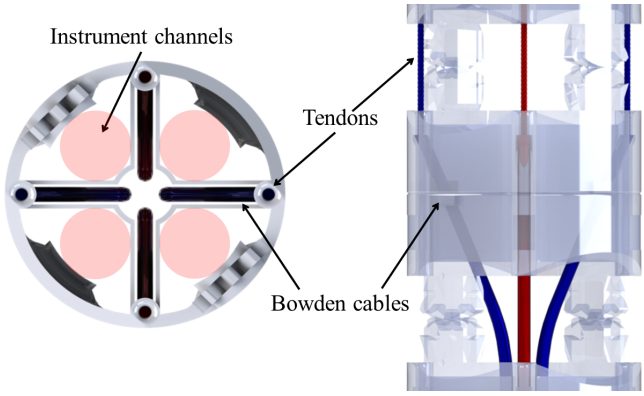

Fig. 6: 'Spinal cord architecture': the Bowden cables and tendons are routed from the center to the outer part of the joint, leaving four internal channels available.

ulation shows that for a floating rolling-joint configuration, the tendon pathway location can significantly reduce the joint range and ultimately the dexterity of the robot which will be further discussed in Section IV.

C. Spinal Cord Architecture

The third challenge of the design of a snake robot for medical applications is to ensure inner space for surgical instruments such as robotic tools, camera, light fibers, suction/irrigation, *etc*. The joint design presented in this document has four instrument channels. This is possible thanks to a 'spinal cord architecture' where the actuation (Bowden cables + tendons) travels through the center position of the joint and are distributed to individual sections as depicted in Fig. 6. This arrangement has two advantages, the first one is that it allows to reduce the wall size of the joint hence increasing the available space for the internal channels. The second advantage is that it keeps the actuation (Bowden cables + tendons) as close as possible to the neutral line (the center of the joint chain has a constant length during motion as explained in [14]) hence reducing tendon cross-talk and the risk of herniation. Finally, because the actuation uses Bowden cables that can slide within the spinal cord architecture, the cross-talk between all the various tendons can be significantly reduced.

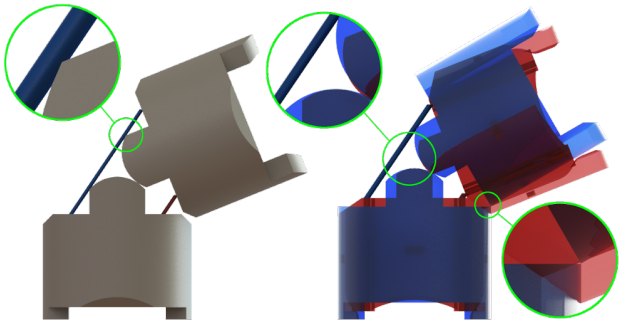

Fig. 7: Collision examples: on the left, tendon-joint collision. On the right, comparison between the initial human made prototype (blue) and the optimized one (red). The optimized rolling-joint has a larger range while preventing collisions.

D. Rolling-Joint Parameters Optimization

The optimization problem is formulated in terms of joint range $\Delta\alpha$ maximization. It has been shown in section III-B that the range of the joint depends on the placement of the tendons. In the following, a constrained optimization for the remaining rolling-joint parameters is described. Again an explorative optimization algorithm is used where the constraint is that the tendons and the joint do not collide as shown in Fig. 7. The joint range $\Delta\alpha$ is a function of the parameters (r, d, D, h) as stated in (10). In an iterative process, the parameters are altered one by one, and for each iteration, the joint angle α is calculated using (8), (9) as objective functions. For each joint parameter, the algorithm will explore the feasible joint range by iteratively simulating a tendon variation while checking for joint limits and tendon-joint collision. Although Fig. 3 shows no possible tendon-joint collision as they are both on a different plane, as the snake robot diameter is decreased (when considering patient-specific design), the risk for collision becomes more important and is therefore considered in the optimization. The algorithm then calculates the rolling-joint width w to ensure joint stability using (11) (a constant value of 0.2 mm is added for mechanical tolerance during manufacturing). The process ends with extracting the optimized joint parameters using (12).

$$\Delta\alpha = f(r, d, D, h) \text{ with } h = 0 \tag{10}$$

$$w = 2\,r\,\sin(\Delta\alpha) + 0.2 \tag{11}$$

$$(r^*, d^*, D^*, h^*) = \arg\max(f) \tag{12}$$

IV. Results

A. Optimization Workflow Results

The complete process of rolling-joint optimization can be summarized in the following optimization workflow. The proposed concept is to offer the possibility to create patient-specific snake robots that can fit into various human anatomies. The process starts with two input requirements: the joint diameter D and the joint length N. In the context of this paper, these parameters were determined using a review on human anatomy from Tugrul *et al.* to match the requirements of a surgical intervention through the esophagus (*e.g.* breathing) when considering an average size adult patient [27]. The identified joint parameters are D=16 mm and N=5.91 mm. This allows two consecutive joints in a straight configuration to pass from the mouth cavity to the oesophagus without colliding with the surrounding organs. Once the input parameters are defined, a Matlab script integrating the algorithm presented in section III-B and III-D computes the optimized joint parameters and feed them via a text file to a computer aided design software equation module such as Solidworks equations. Subsequently, a template rolling-joint design shown in Fig. 3 is automatically updated with the computed parameters and can be rapidly manufactured using 3D printing. The results of the optimization are compared to an older robot prototype that was manually designed and are

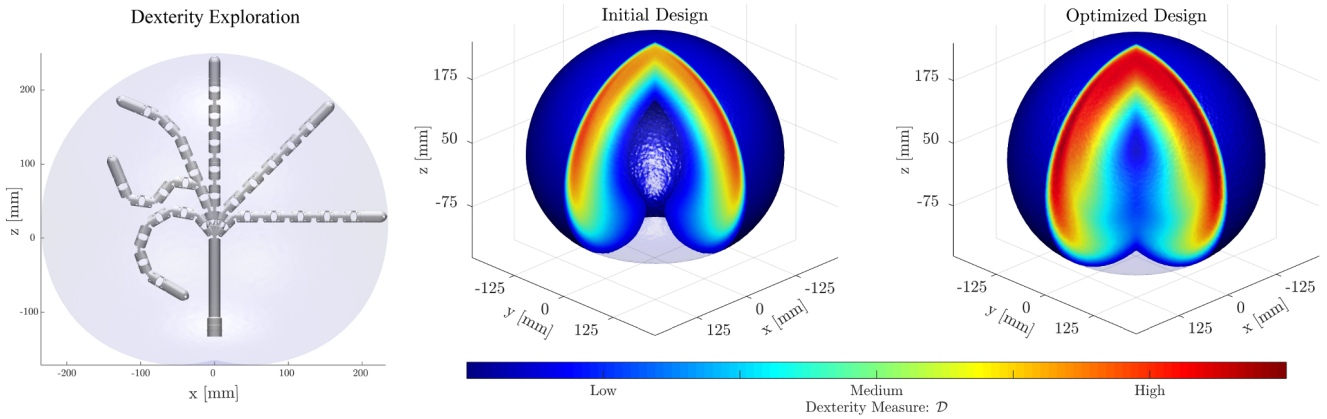

Fig. 8: Dexterous workspace analysis. This figure compares a first made prototype and the optimized version. The optimized version shows an overall better dexterity, a larger high dexterity region and a more complete workspace.

further analyzed in the following paragraphs. $\Delta\theta$ represents the overall joint range.

B. Clinical Validation

The relevance of the proposed design for ENT clinical applications was validated in a simulated environment using a virtual simulator presented in [28]. The proposed device is composed of three actuated sections, each section is composed of two subsections of floating rolling-joints as depicted in Fig. 3 and its kinematic was thoroughly investigated in [28]. The proposed joint arrangement allows for a large range of joint configurations, from straight shapes to S shapes as shown in Fig. 8. The results shown in Fig. 9 show that the proposed snake robot design can reach surgical sites such as the left and right tonsils, the back of the tongue and even deeper seated organs at the bottom of the throat.

C. Workspace Analysis

The optimized joint design has an immediate impact on the workspace of the robot. Although the reachable workspace is only increased by a small amount the dexterity of the robot in the workspace increased significantly. Operating the robot in regions of high dexterity is important to successfully execute a task [29], and hence a large dexterous workspace is crucial. A common technique for analyzing the dexterity is to calculate the manipulability $(\mathcal{M})$, which is the product of the singular values of the Jacobian (J), an alternative measure is the inverse conditional number $(\mathcal{C})$, the quotient of smallest to largest singular value. Since the dexterity of the robot does not only depend on the Jacobian but also on other factors such as joint limits or collisions, the dexterity $(\mathcal{D})$ is commonly calculated by multiplying a penalty depending on these additional factors. A standard technique is presented in [30] however, for redundant robots as the presented snake-like robot, a single joint in the limits would result in a dexterity measure of zero, although other joints would be able to fully compensate the lost DOF. The approach in [29] accounts for redundant manipulators however at the cost of 2^6 singular-value-decompositions per configuration. Therefore, the method used is to penalize the Jacobian column-wise,

$$\mathcal{P}_i^q = \frac{1 - \exp\{\frac{4\mathcal{K}_q(q_i - q_{i,min})(q_{i,max} - q_i)}{(q_{i,max} - q_{i,min})^2}\}}{1 - \exp\{\mathcal{K}_q\}} \tag{13}$$

with $\mathcal{P}_i^q$ the penalization term for the i^{th} joint, $q_{i,min}, q_{i,max}$ the joint limits, and $\mathcal{K}_q$ a scaling constant. $\mathcal{P}_i^q$ is then used to compute the joint limit constrained Jacobian (J^q),

$$j_i^q = \mathcal{P}_i^q j_i \text{ with } J^q = [j_1, j_2, \cdots, j_{n_q}] \tag{14}$$

where j_i, j_i^q are the i^{th} Jacobian and constrained Jacobian columns respectively and which leads to a dexterity measure $\mathcal{D}$ that takes the compensation capabilities of redundant manipulators into account:

$$\mathcal{D} = \sqrt{\left|J^q J^{q^T}\right|} = \prod_{i=1}^{n_q} \sigma_i^q, \tag{15}$$

where σ_i^q are the singular values of J^q. The maximum achievable dexterity within a discrete volume is visualized in Fig. 8. It shows that the optimized snake design with increases joint range has a significantly larger high dexterity workspace. This is numerically quantified by assessing the volume of high dexterity as depicted in Fig. 8.

TABLE I: Comparison of Manual and Optimized Results

	r (mm)	$d_{bot/top}$ (mm)	D (mm)	N (mm)	w (mm)	$\Delta\theta$ (rad)
Manual	4	7.19/3.5	16	5.91	4.5	2.10
Optimized	3.09	5.66/5.66	16	5.91	3.77	2.39

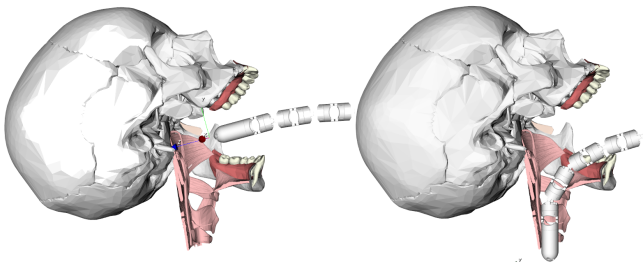

Fig. 9: Simulation of the *i²Snake* insertion through the mouth. The robot can reach all the way down the throat without colliding with surrounding organs.

TABLE II: Repeatability Characterization

Repeatability Characterization	**Precision Measurement** Start point error	End point error
Vertical motion	0.92 mm	1.37 mm
Horizontal motion	2.10 mm	4.17 mm

D. Prototype Characterization

A prototype of the optimized joint was manufactured using a Mlab metal 3D printer (Conceptlaser, Lichtenfels, Germany). The following section describes the characterization of this optimized device and compares it to a previously manually designed prototype.

1) Repeatability Characterization: The repeatability of a robotic device refers to its capacity to reach the same configurations with the smallest error possible. As this paper focuses on the design rather than the control, the accuracy was not investigated. Capstan and tendon driven robots are known to have backlash during motion. This is due to the elasticity properties of the cables, the material, the braiding pattern, *etc*. This phenomenon is even more observable when using Bowden cables combined with tendons as they tend to compress as the tendons stretch, resulting in increased backlash. For the purpose of this paper, a linear backlash compensation was implemented consisting of adding a constant value when the motor changes direction (feed-forward control). The preset constant values were characterized manually for each motor. The repeatability error of the snake robot was characterized by doing a repetitive motion. Two directions of motion are investigated: vertical (XZ) and horizontal (XY) motion. The robot was controlled in joint space, moving back and forth between two joint values situated halfway of the full joint range. The position was measured at the tip of the robot, using a 3D Guidance trakSTAR electromagnetic tracker (Ascension Technology, USA), which has a resolution of 1.4 mm RMS. The motors used for actuation are 12 W motor, model: EC13 coupled with a GP13A gearbox (Maxon Motors, Switzerland). The repeatability characterization setup is shown in Fig. 10. The results are presented in Table II. Over 18 repeated motions, the resulting standard deviation varies from 0.92 mm to 4.17 mm. Depending on the motion direction (going one way or returning to the initial joint position) a hysteresis in the resulting tip trajectory could be observed. This shows that a linear backlash compensation is not enough to correctly compensate the tendon elongation and Bowden cable compression, and that more complex models are required. Overall the repeatability results are

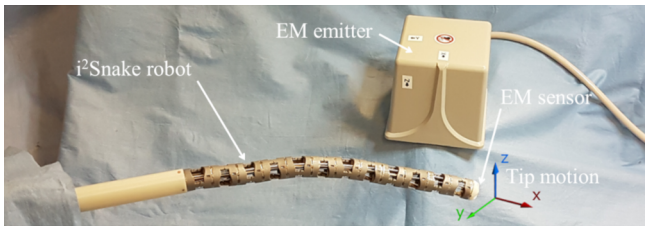

Fig. 10: The position tracking rig. The electromagnetic sensor is located inside the end effector of the robot. As the robot moves, the head is tracked in absolute position.

TABLE III: Force Characterization

Force Characterization	**Force Measurement** Proximal section	Middle section	Distal section
Max. force (z axis)	4.34 N	2.02 N	1.99 N
Max. force (norm)	5.58 N	4.74 N	2.16 N

sufficient for a teleoperation scenario where the surgeons can visually compensate for the error, but a more complex control scheme would be required for autonomous navigation.

2) Manipulation Forces: One of the challenges of surgical robots is to have a compact design while ensuring manipulation forces large enough for tissue manipulation. The manipulation force of the snake robot was evaluated in a worst case configuration. The body of the snake robot was fully extended, which results in the maximum lever length in a horizontal position. The motion direction was upwards, opposing gravity, and each of the three sections of the snake robot was characterized. The characterization consisted of moving the robot upwards until reaching a preset current limit. Limiting the current avoids breakage of any of the mechanical components such as tendons, capstans, *etc*. The force sensor used was an ATI Mini40 (ATI Industrial, USA) which has a force range of 20N with a 10mN resolution on the z-axis. The sensor value was retrieved using a PCI-6220 data acquisition interface (National Instruments, USA). A picture of the setup is shown in Fig. 11. The resulting forces for each section are plotted in Fig. 12 and summarized in Table III. The norm of the force vector for each section was also plotted. The difference between the force along the z-axis and the norm of the force is mainly due to the bending of the body of the snake robot. During the experiment, as only the tip of the robot was constrained by the force sensor, the rest of the body would slightly bend downward, resulting in a slight tilt of the contact point between the body and the sensor. This lead to pulling forces along the x-axis (aligned along the body of the robot). This behavior is visible in the middle section plot where the difference between the force along the z-axis and the norm is significant. The resulting force at the tip of the robot reaches 2 N which is an encouraging result but will need further investigations whether this is sufficient for tissue handling.

V. CONCLUSIONS

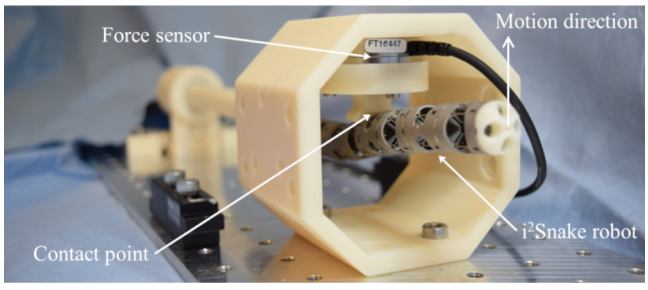

Fig. 11: The force characterization rig. Each section was characterized using a 6 axis force sensor. The force was measured with the body of the snake fully extended, moving upward and opposing gravity.

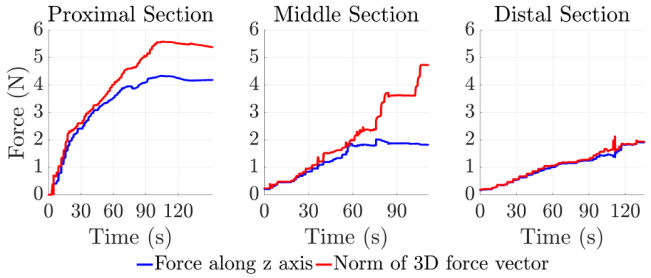

Fig. 12: Force characterization. The force along the z axis and the norm of 3D force vector were measured for each section. The resulting force at the tip reaches 2N.

This paper introduces a novel multi-channel redundant snake-like robot for minimally invasive surgery. The key technical contributions of the work include a new bi-stable synchronous rolling-joint, a corresponding optimization algorithm that also consider collisions, and a spinal cord architecture with tendon routed in the center of the robot to reduce tendon cross-talk. The model of the rolling-joint for 3D motion is investigated, and the details of the algorithm to optimize the joint parameters are described. The resulting dexterity of the proposed device was studied in detail, demonstrating marked improvements compared to a previous prototype. An optimized joint was manufactured using additive manufacturing and characterized in terms of precision and manipulation forces. The results show manipulation forces up to 5.6 N but will need to be further characterized in a clinical scenario with an outer sheath and tools running inside the robot. Future work will investigate non-linear control for backlash and elongation compensation in the context of autonomous navigation. Flexible and exchangeable surgical tools will be integrated and tested during *ex-vivo* and ultimately *in-vivo* surgical tasks.

ACKNOWLEDGMENT

The author would like to thank Gauthier Gras and Piyamate Wisanuvej for their input on force and position sensing.

REFERENCES

[1] V. Vitiello, S. L. Lee, T. P. Cundy, and G. Z. Yang, "Emerging robotic platforms for minimally invasive surgery," *IEEE Rev Biomed Eng*, vol. 6, pp. 111–26, 2013.

[2] H. M. Le, T. N. Do, and S. J. Phee, "A survey on actuators-driven surgical robots," *Sensors and Actuators A: Physical*, vol. 247, pp. 323–354, 2016.

[3] N. Patel, C. A. Seneci, J. Shang, K. Leibrandt, G.-Z. Yang, A. Darzi, and J. Teare, "Evaluation of a novel flexible snake robot for endoluminal surgery," *Surgical Endoscopy*, vol. 29, no. 11, pp. 3349–3355, 2015.

[4] J. Burgner-Kahrs, D. C. Rucker, and H. Choset, "Continuum robots for medical applications: A survey," *IEEE Trans. on Rob.*, vol. 31, no. 6, pp. 1261–1280, 2015.

[5] C. A. Seneci, J. Shang, K. Leibrandt, V. Vitiello, N. Patel, A. Darzi, J. Teare, and G.-Z. Yang, "Design and evaluation of a novel flexible robot for transluminal and endoluminal surgery," in *IEEE/RSJ Int. Conf. on Intel. Rob. & Sys.* IEEE, 2014, pp. 1314–1321.

[6] Y. Chen, J. Liang, and I. W. Hunter, "Modular continuum robotic endoscope design and path planning," in *IEEE Int. Conf. on Rob. & Auto.* IEEE, 2014, pp. 5393–5400.

[7] J. Shang, D. P. Noonan, C. Payne, J. Clark, M. H. Sodergren, A. Darzi, and G. Z. Yang, "An articulated universal joint based flexible access robot for minimally invasive surgery," in *IEEE Int. Conf. on Robot. & Autom.*, 2011, pp. 1147–1152.

[8] J. Shang, C. J. Payne, J. Clark, D. P. Noonan, K. W. Kwok, A. Darzi, and G. Z. Yang, "Design of a multitasking robotic platform with flexible arms and articulated head for minimally invasive surgery," in *IEEE/RSJ Int. Conf. on Intel. Rob. & Sys.*, 2012, pp. 1988–1993.

[9] M. Cianchetti, T. Ranzani, G. Gerboni, I. De Falco, C. Laschi, and A. Menciassi, "Stiff-flop surgical manipulator: mechanical design and experimental characterization of the single module," in *IEEE/RSJ Int. Conf. on Intel. Rob. & Sys.* IEEE, 2013, pp. 3576–3581.

[10] C. Liu and W.-H. Liao, "A snake robot using shape memory alloys," in *IEEE Int. Conf. on Rob. & Bio.* IEEE, 2004, pp. 601–605.

[11] P. Dupont, J. Lock, B. Itkowitz, and E. Butler, "Design and control of concentric-tube robots," *IEEE Trans. on Rob.*, vol. 26, no. 2, pp. 209–225, 2010.

[12] H.-S. Yoon and B.-J. Yi, "Design of a master device for controlling multi-moduled continuum robots," *Proc. of the Instit. of Mech. Eng.*, p. 0954406215625359, 2015.

[13] T.-D. Nguyen and J. Burgner-Kahrs, "A tendon-driven continuum robot with extensible sections," in *IEEE/RSJ Int. Conf. on Intel. Rob. & Sys.*, 2015, pp. 2130–2135.

[14] Y. J. Kim, S. B. Cheng, S. Kim, and K. Iagnemma, "A stiffness-adjustable hyperredundant manipulator using a variable neutral-line mechanism for minimally invasive surgery," *IEEE Trans. on Rob.*, vol. 30, no. 2, pp. 382–395, 2014.

[15] V. Agrawal, W. J. Peine, and B. Yao, "Modeling of a closed loop cable-conduit transmission system," in *IEEE Int. Conf. on Rob. & Auto.* IEEE, 2008, pp. 3407–3412.

[16] K. Leibrandt, P. Wisanuvej, G. Gras, J. Shang, C. A. Seneci, P. Giataganas, V. Vitiello, A. Darzi, and G. Z. Yang, "Effective manipulation in confined spaces of highly articulated robotic instruments for single access surgery," *IEEE Robot. and Autom. Lett.*, vol. 2, no. 3, pp. 1704–1711, 2017.

[17] C. A. Seneci, K. Leibrandt, P. Wisanuvej, J. Shang, A. Darzi, and G. Z. Yang, "Design of a smart 3d-printed wristed robotic surgical instrument with embedded force sensing and modularity," in *IEEE/RSJ Int. Conf. on Intel. Rob. & Sys.*, 2016, pp. 3677–3683.

[18] P. Berthet-Rayne, G. Gras, K. Leibrandt, P. Wisanuvej, A. Schmitz, C. A. Seneci, and G.-Z. Yang, "The i^{2}snake robotic platform for endoscopic surgery." *Annals of Biomed. Engineer. 10.1007/s10439-018-2066-y*, 2018.

[19] P. Berthet-Rayne and G.-Z. Yang, "Vision based shape reconstruction of tendon driven snake-like surgical robots," in *Hamlyn Symp. on Med. Robot.*, vol. 10, London, 2017.

[20] A. Jeanneau, J. Herder, T. Laliberte, and C. Gosselin, "A compliant rolling contact joint and its application in a 3-dof planar parallel mechanism with kinematic analysis," in *ASME Int. Des. Engin./Comp. & Info. Techn. Conf.* American Soc. of Mech. Engin., 2004, pp. 689–698.

[21] C. L. Collins, "Kinematics of robot fingers with circular rolling contact joints," *Journal of Robotic Systems*, vol. 20, no. 6, pp. 285–296, 2003.

[22] F. Jelinek, R. Pessers, and P. Breedveld, "Dragonflex smart steerable laparoscopic instrument," *Journal of Medical Devices-Transactions of the Asme*, vol. 8, no. 1, p. 015001, 2014.

[23] J. W. Suh, K. Y. Kim, J. W. Jeong, and J. J. Lee, "Design considerations for a hyper-redundant pulleyless rolling joint with elastic fixtures," *IEEE-Asme Trans. on Mecha.*, vol. 20, no. 6, pp. 2841–2852, 2015.

[24] T. Cooper, D. Wallace, S. Chang, S. Anderson, D. Williams, and S. Manzo, "Surgical tool having positively positionable tendon-actuated multi-disk wrist joint," Patent WO2 003 001 986A2, 2003.

[25] M. Williams, "Instrument wrist with cycloidal surfaces," Patent US20 110 152 879 A1, 2011.

[26] R. Buckingham, "Snake arm robots," *Industrial Robot: An International Journal*, vol. 29, no. 3, pp. 242–245, 2002.

[27] T. T. Kararli, "Comparison of the gastrointestinal anatomy, physiology, and biochemistry of humans and commonly used laboratory-animals," *Biopharma. & Drug Disposition*, vol. 16, no. 5, pp. 351–380, 1995.

[28] P. Berthet-Rayne, K. Leibrandt, G. Gras, P. Fraisse, A. Crosnier, and G. Z. Yang, "Inverse kinematics control methods for redundant snake-like robot teleoperation during minimally invasive surgery," *IEEE Robot. and Autom. Lett.*, vol. 3, no. 3, pp. 2501–2508, 2018.

[29] N. Vahrenkamp and T. Asfour, "Representing the robots workspace through constrained manipulability analysis," *Autonomous Robots*, vol. 38, no. 1, pp. 17–30, 2015.

[30] M. J. Tsai and Y. H. Chiou, "Manipulability of manipulators," *Mechanism and Machine Theory*, vol. 25, no. 5, pp. 575–585, 1990.